Mechanism of Flame Stabilization in Turbulent, Lifted-Jet Flames

R. W. SCHEFER* and P. J. GOIX

Combustion Research Facility, Sandia National Laboratories, Livermore, CA 94551-0969

Particle image velocimetry was used to study the velocity field in the stabilization region of lifted, turbulent CH_4-jet flames over a range of Reynolds numbers from 7000 to 19,500. Measured velocities at the flame base are considerably below the turbulent flame speeds derived from previous studies and show a dependence on the Reynolds number. The average velocity at the stabilization point is nearly a factor of five below the premixed laminar burning velocity at the lowest Reynolds number and asymptotes to a value about 20% higher as the Reynolds number is increased. Planar images of OH show that the flame zone structure near the stabilization point is also highly dependent on the Reynolds number. Comparison of the present OH images with previous CH_4 Raman imaging results shows that the flame thickness is determined by the width of the flammable region. At a low Reynolds number, the flame is stabilized near the jet exit where the flammable layer is thin, resulting in a thin flame zone. At an increased Reynolds number, the stabilization point is located farther downstream where the flammable region is wider, resulting in a correspondingly wider flame zone. It is proposed that the lower velocities observed at the flame base are related to thinning of the flame zone at low Reynolds, which results in greater curvature of the flame base. The increased flame curvature effectively defocuses the transport of heat and flame radicals to reactants upstream of the propagating flame front, resulting in reduced burning velocities. The implications of these results for mechanisms controlling turbulent flame stabilization, with an emphasis on the applicability of triple flame concepts to turbulent flows, are discussed.

INTRODUCTION

Flame stabilization is an issue of considerable fundamental importance to turbulent combustor design. This importance is highlighted by the recent emphasis on low NO_x burners, where flame stability is often adversely affected by NO_x reduction strategies. Flame stabilization theories generally recognize the importance of local ignition, flame propagation, extinction, and reignition phenomena as factors controlling flame stability. These theories have in large part been developed based on experimental observations in turbulent, lifted-jet flames. Lifted flames include many of the fundamental mechanisms controlling flame stabilization in practical burners, yet are also well-characterized fluid dynamically.

Theories for lifted flame stabilization have been reviewed by Pitts [1]. Early theories were based on the concept of premixed flame propagation. Vanquickenborne and van Tiggelen [2] proposed that in lifted flames the fuel and air are premixed prior to ignition and that stabilization occurs where the local flow velocity along the stoichiometric contour is equal to the turbulent flame speed. Based on time-averaged velocity data, and the assumption that the turbulent burning velocity, S_T, equals the time-averaged gas velocity at the stabilization point, a relation was obtained for S_T as a function of turbulence intensity and turbulence scale. Measurements showed that S_T can be up to four times higher than the premixed laminar flame speed over the range of conditions studied. Flame extinction forms the basis for several more recent theories. Peters and Williams [3] have argued that the fuel and air are not premixed at the flame stabilization point and that liftoff can be explained in terms of laminar flamelets in which extinction occurs where the local value of scalar dissipation exceeds a critical value and the flame is quenched. The flame is stabilized where scalar dissipation is below this critical value. Extinction has also been proposed by Byggstoyl and Magnussen [4] as the mechanism controlling flame stabilization. In this model, stabilization is determined by extinction at the smallest turbulence scales.

Previous single-shot images of the instantaneous CH and CH_4 distributions in lifted, turbulent CH_4-jet flames were used to evaluate

*Corresponding author.

COMBUSTION AND FLAME 112:559–574 (1998)

Published by Elsevier Science Inc.

0010-2180/98/$19.00
PII S0010-2180(97)00130-2

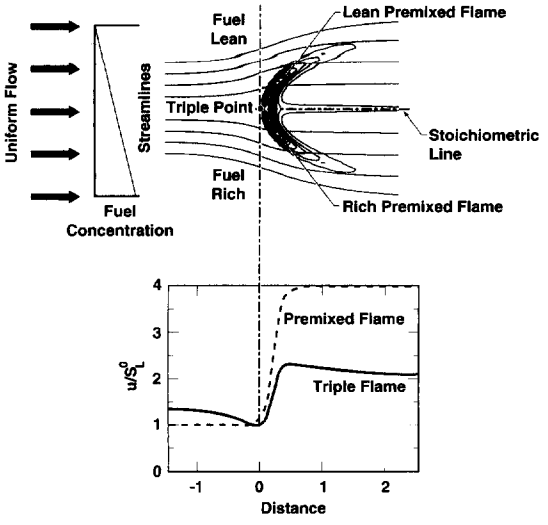

Fig. 1. Schematic of a laminar triple flame propagating into a fuel concentration gradient. Flame structure is indicated by isocontour line of reaction rate. The bottom graph shows profiles of the horizontal velocity component along stoichiometric line for a propagating triple flame (—) and a planar premixed flame (- - -). From Ruestch et al. [7].

current theories on lifted-flame stabilization [5]. It was found that local stoichiometry, and not scalar dissipation, is the primary factor controlling flame stability. Specifically, the fuel and air were found to be premixed and near stoichiometric conditions at the flame stabilization point, which is consistent with premixed flame propagation concepts [2]. In a subsequent paper, a double-pulse technique for simultaneous CH and CH_4 imaging was developed to study the temporal evolution of flame interactions with vortical structures in the lifted flame [6]. The results showed that interactions between these vortical structures and the flame play an important role in flame stabilization. Extinction was found to occur along both the downstream edge of the vortices and on the upstream side. Once the flame is extinguished, the stabilization point can be carried significant distances downstream by the vortex. The return to an upstream stabilization location occurs through turbulent premixed flame propagation with minimal vortex interaction.

A current question of much interest is whether triple-flame concepts are relevant to flame propagation in turbulent reacting flows [7, 8]. As shown in Fig. 1, triple flames occur when a flame propagates through a fuel concentration gradient. In the case shown, the flow is uniform and the fuel/air mixture varies from a fuel-lean mixture on the top to a fuel-rich mixture on the bottom. Near the center, a stoichiometric mixture of fuel and air exists. This situation results in the formation of a fuel-lean premixed flame branch extending toward the top and a fuel-rich premixed flame branch extending toward the bottom. These branches are curved since the flame speed decreases as the mixture moves farther away from stoichiometric conditions. A diffusion flame also forms behind the premixed flame branches along the stoichiometric line. This diffusion flame is supported by excess air from the lean premixed flame branch and excess fuel from the rich premixed flame branch. Farther downstream, fuel and air from outside the premixed flame envelope diffuse inward and further support the diffusion flame.

An important characteristic of triple-flame behavior is that the flow streamlines diverge upstream of the propagating flame. This is shown in Fig. 1, where the streamlines diverge as the flow approaches the leading edge of the triple flame. Calculations have shown that this divergence is due to acceleration of the velocity component normal to the premixed flame branches, which requires that the flow upstream diverges. The bottom graph in Fig. 1 shows the variation of the axial velocity component, normalized by the planar premixed laminar burning velocity, S_L, along the stoichiometric line. Shown for comparison is the velocity profile through a planar premixed laminar flame. With the triple flame, the upstream flow velocity decelerates due to divergence as the flame is approached and reaches a value equal to S_L at the flame leading edge. The flow then accelerates across the flame due to volume expansion and asymptotically approaches a downstream value that depends on the gas density ratio across the flame.

The applicability of the triple-flame concept to lifted-flame stabilization was recently explored by Muniz and Mungal [9]. In that work, planar imaging velocimetry (PIV) was used to study the velocity field at the base of turbulent, lifted methane and ethylene jet diffusion flames in coflow air. A range of Reynolds numbers from 3800 to 22,000, with coflow air velocities

between 0.27 m/s and 1.85 m/s, were studied. The results showed that the flame base is stabilized primarily in low-velocity regions of the jet. They further found that conditional velocities at the flame base are typically less than three times the laminar flame speed. Since these measured velocities are considerably below previously determined turbulent flame speeds, it was suggested that turbulent flame speed concepts are not representative of stabilization physics and should be reexamined. It was concluded that at the flame base the results were consistent with the presence of a leading-edge flame with characteristics similar to a triple flame.

The present paper is intended to both confirm and extend this previous work by Muñiz and Mungal. The present study considers a free jet into ambient air with no coflow. The measurements were obtained in flames studied previously so that the results of these previous studies can aid in the interpretation of the present results. The Reynolds number range considered by Muñiz and Mungal was extended to a higher Reynolds number of 19,500 in the methane flames. In addition, Planar Laser-Induced Fluorescence (PLIF) imaging measurements of the OH radical were obtained to provide information on the flame structure in the stabilization region. In the remainder of the paper, the experimental system will be described and selected experimental results will be presented. The PIV data will first be presented and used to characterize the velocity statistics at the instantaneous flame stabilization point. Planar images of the OH distribution will then be used to describe variations in flame zone structure with Reynolds number. Finally, the implications of the results with respect to the existence of triple flames in these flows will be examined.

EXPERIMENTAL SYSTEM

Burner Description and Flow Conditions

The burner consisted of a 5.4-mm diameter fuel jet located in the center of a plate. Methane was injected through the central fuel tube into surrounding still air. Measurements were obtained at jet exit velocities of 21, 37, and 60 m/s, corresponding to jet exit Reynolds numbers of 7,000, 12,000, and 19,500, respectively. These jet exit velocities are well below the flame blowout velocity of about 90 m/s. Photographs of the lifted flames studied are shown in Fig. 2. At the lowest jet velocity (Fig. 2a), the visible flame is lifted and stabilized at an axial position, x, approximately 30 mm downstream of the burner face. The upstream part of the flame is blue and becomes yellow due to soot formation farther downstream. At the higher velocity of 37 m/s (Fig. 2b), the flame is stabilized farther downstream at an average liftoff height of 80 mm. The flame is blue over its entire extent with no visible soot formation. The visible flame at 60 m/s (not shown) is nearly identical to Fig. 2b except that the average lift-off height is 135 mm.

Particle Image Velocimetry System

A schematic of the Particle Image Velocimetry (PIV) system is shown in Fig. 3. The technique uses the 532-nm output of a double-pulsed Nd:YAG laser to illuminate Al_2O_3 seed particles (nominal 0.3 μm diameter) added to the flow. With this double-pulse option the time delay between pulses could be varied from 15 μs to 200 μs. Typically, a laser power of 65 mJ/pulse was found sufficient for the measurements. The laser beam is formed into a sheet approximately 250-μm thick using cylindrical optics and subsequently passed through the test section. Mie-scattered light from the seed particles is detected using a CCD video camera with a 1000 $\times$ 1000 pixel array (TSI Model 630045 Cross-correlation Camera). Particle images corresponding to the two laser pulses are recorded on sequential video frames using a frame straddle technique. Average particle displacement is calculated from the images using a cross correlation analysis and the velocity is then determined from this displacement and the known time between laser pulses. In all data reduction calculations, 32 pixels per interrogation spot were used, with the spot size variable depending on the size of the imaged field-of-view. For full-field images (50 $\times$ 50 mm field-of-view), this gave an interrogation volume of 1.6 $\times$ 1.6 $\times$ 0.25 mm. For the 20 $\times$ 20 mm field-of-view used to determine the velocities in the region of the flame stabilization point, the

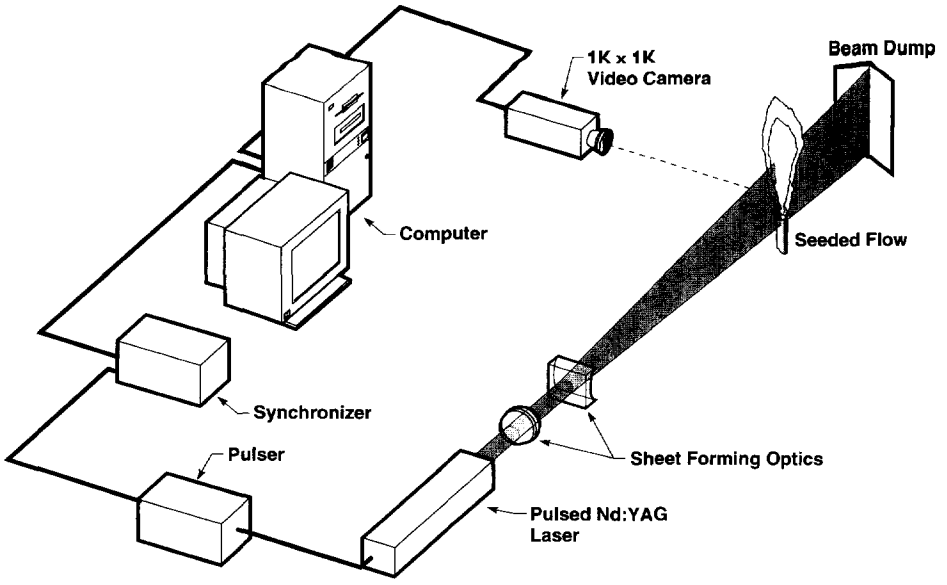

Fig. 3. Schematic of planar imaging velocimetry system.

interrogation volume was 0.65 × 0.65 × 0.25 mm.

Seed particles in the fuel jet were supplied by a fluidized bed seeder. A cyclone separator located after the seeder effectively removed particle agglomerates and provided a more uniform size distribution. The addition of seed particles to the surrounding air was more difficult since it was desired to study the behavior of a free jet, i.e., a jet into still air. Several approaches were tried to determine the most effective method of adding seed particles to the air. Initially, the use of coflow air was considered. Visual observations showed that for air-to-jet velocity ratios, U_a/U_j, less than 0.002 no change in flame lift-off height was observed (the jet lift-off height increased significantly with increasing air velocity once this velocity ratio was exceeded). Velocity measurements further showed that below this velocity ratio the jet behaved essentially as a free jet. The main difficulty with this approach was found to be operation of the fluidized bed seeder at the required low air flow rates, where it was often difficult to maintain sufficiently high seed densities in the air stream.

An alternative approach was to ignite the flame with a sufficiently high coflow air velocity to obtain a high seed density in the air stream. Once steady state was reached, the air flow was rapidly shut off. Observations showed that while the flame returned to steady state within about one second, the settling time for the seed particles in the air was significantly longer. Thus, the seed particles remained in the air surrounding the jet for several seconds, during which time they were entrained into the fuel jet. The particle images were obtained during the time interval in which the lifted flame had achieved steady state and there was sufficient seed particles in the entrained air. Radial and axial velocity profiles obtained by averaging the images showed good agreement with the expected free jet behavior. The latter approach was used to obtain the data reported in the remainder of the paper.

The delay time between particle images was found to be an important parameter due to the large range of velocities in each image. For example, the velocities typically range from several tens of m/s in the central jet to velocities on the order of a tenth of a m/s near the flame base. For a given spatial resolution (i.e., interrogation spot size), particle travel between images must be limited to a distance on the order of the resolution. The approach taken was to limit the size of region imaged, thus reducing the range of velocities measured for a given delay time. Typical delay times between pulses

were 15 μs in the central jet to nearly 200 μs in the lower velocity flame stabilization region.

The long-term repeatability of the measurements was established by repeating the measurements after the initial data set was obtained. The estimated uncertainties in the velocity were determined from calibration measurements in a laminar air flow exiting through a 50-mm diameter nozzle. From these measurements, the experimental uncertainty in velocity was estimated over a range of velocities consistent with those measured in the lifted flame experiments to be better than $\pm 1\%$.

OH Imaging System

The ultraviolet laser radiation for excitation of the OH molecule was provided by a frequency-doubled, Nd:YAG-pumped dye laser. The beam (8-ns pulse duration, 0.3-cm^{-1} line width) was used to pump the $Q_1(8)$ transition ($v'' = 0 \rightarrow v' = 1$) of the OH $A^2\Sigma$-$X^2\Pi$ electronic band at 283.5 nm. Selection of the $Q_1(8)$ line was based on a compromise between sufficient signal strength and sensitivity to temperature of the fractional population within the absorbing level. The laser-pumped $Q_1(8)$ line has a population fraction that varies by only 10% over the temperature range 1000 K to 2300 K. The OH fluorescence signal was collected using a 105-mm focal length, f/4.5 UV Nikkor lens, passed through a 10-nm bandwidth filter centered at 312 nm, and focused onto a cooled CCD camera. The camera was gated for 1 μs using an image diode located in front of the camera, which encompassed the 8-ns pulse duration of the dye-laser beam. The camera detector was operated in a 1 K $\times$ 1 K pixel format, providing a spatial resolution of 60 $\times$ 60 μm at the image plane. This resolution compares with Kolomogorov scales of 0.2 and 0.7 mm, which were estimated at the minimum and maximum average lift-off heights of 30 and 135 mm, respectively, for the flames studied.

The laser sheet for the OH fluorescence was formed by a cylindrical/spherical lens combination, which was used to produce a sheet 60 mm high and 250 μm thick. With an laser power of 5 mJ/pulse, the resulting average spectral power density is about 1.9×10^7 (watts/cm^{-1})/cm^2. This is within the linear fluorescence regime where the fluorescence signal depends on the collisional quenching rate and is a linear function of laser power. The collisional quenching rate term is a function of temperature, pressure, and gas composition, which are typically not known in turbulent flames. Barlow et al. [10] used strained laminar flame calculations for air-diluted CH_4 fuel mixtures to evaluate the importance of corrections for quenching and ground state population fraction in the linear fluorescence regime. The calculations were carried out over a range of strain rates for rotational levels of N = 6 and N = 8. In general, it was concluded that linear LIF can be used to measure OH concentration in these flames to good accuracy without corrections for quenching and population fraction. At low values of strain, the combined corrections due to quenching and population fraction variations across the flames were less than 5% of the maximum OH concentration. At higher strain rates approaching extinction, the combined corrections were less than 20%. These error estimates are expected to be indicative of the errors in the present measurements. Note that no attempt is made to quantify the present OH concentration measurements through calibration. Rather, the OH images are presented to visualize the flame zone structure in the region of flame stabilization. Given the modest errors in the relative OH concentration levels, the visualizations are expected to be fully representative of the actual flame structure.

RESULTS

Velocity Field

Shown in Fig. 4 is a typical particle Mie scattering image (left) and the corresponding velocity vector field (right). The Mie scattering image shows a relatively uniform particle distribution across most of the field. The notable exceptions are the two narrow regions located toward the upper half of the image where the seed density is considerably less. These regions indicate the high-temperature zones where the gas density is nearly a factor of 7 less than in the nonreacting flow [5, 9, 11]. The two regions correspond to the two sides of the flame located in the mixing

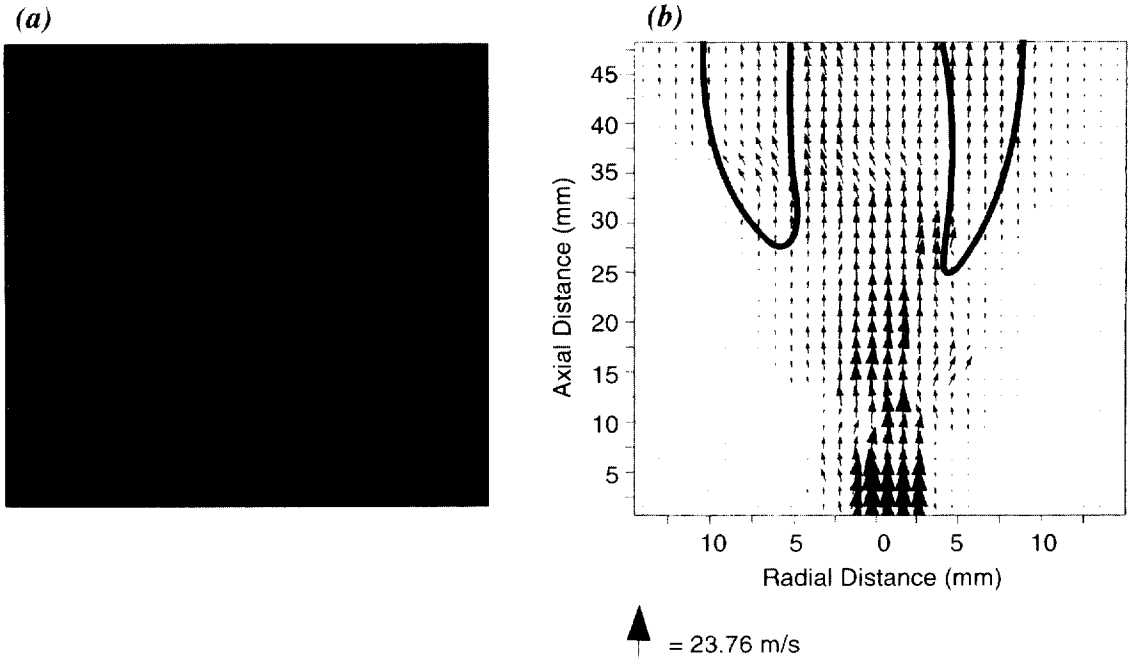

Fig. 4. Particle Mie scattering image (left) and corresponding velocity vector field (right). Jet Reynolds number = 7000. Correspondence between vector length and velocity magnitude is indicated by the vector located below the figure. Regions enclosed by heavy solid lines and originating from top of velocity vector field indicate high temperature zones.

region adjacent to the fuel-rich, nonreacting central jet. The decrease in particle density can be used as a marker for the high temperature zone and can be used to condition the velocity statistics [9, 11]. An outline of the low-density flame region has been superimposed on the velocity vector field shown to the right. The velocity vectors indicate both flow direction and velocity magnitude. As expected, the highest velocities exist in the central region of the jet and decrease moving into the mixing region adjacent to the jet. The velocity also decreases in the downstream direction due to shear between the fuel jet and outer ambient air. The instantaneous central jet flow presents a somewhat random, meandering appearance that differs considerably from the time-averaged jet appearance. Similar observations were made in lifted flames with coflow air [9].

Two typical instantaneous velocity vector fields in the region of the flame stabilization point are shown in Fig. 5. Note that the field of view has been reduced and is confined to the low velocity mixing region along the left side of the central jet to circumvent dynamic range limitations of the PIV system. Again the region corresponding to the high-temperature zone has been outlined. The most upstream location of the high-temperature flame region will hereafter be used to define the flame stabilization point, or flame base. In the image on the left, velocities immediately upstream of the flame stabilization point are typically less than 0.4 m/s. Divergence of the flow as the flame base is approached is also evident. Noteworthy is the presence of a counterclockwise-rotating vortex centered approximately 2 mm upstream and slightly toward the right of the flame base. Previous double-pulse images of CH/CH_4 have shown that such interactions between vortical structures and the flame lead to outward bulges in the flame and local extinction due to the high strain rates at the vortex leading edge [6]. The flame stabilization point is often carried considerable distances downstream by the vortex before the strain rates decrease sufficiently for the flame to propagate around the vortex and return upstream.

The velocity vector field on the right corresponds to another instant in time and again

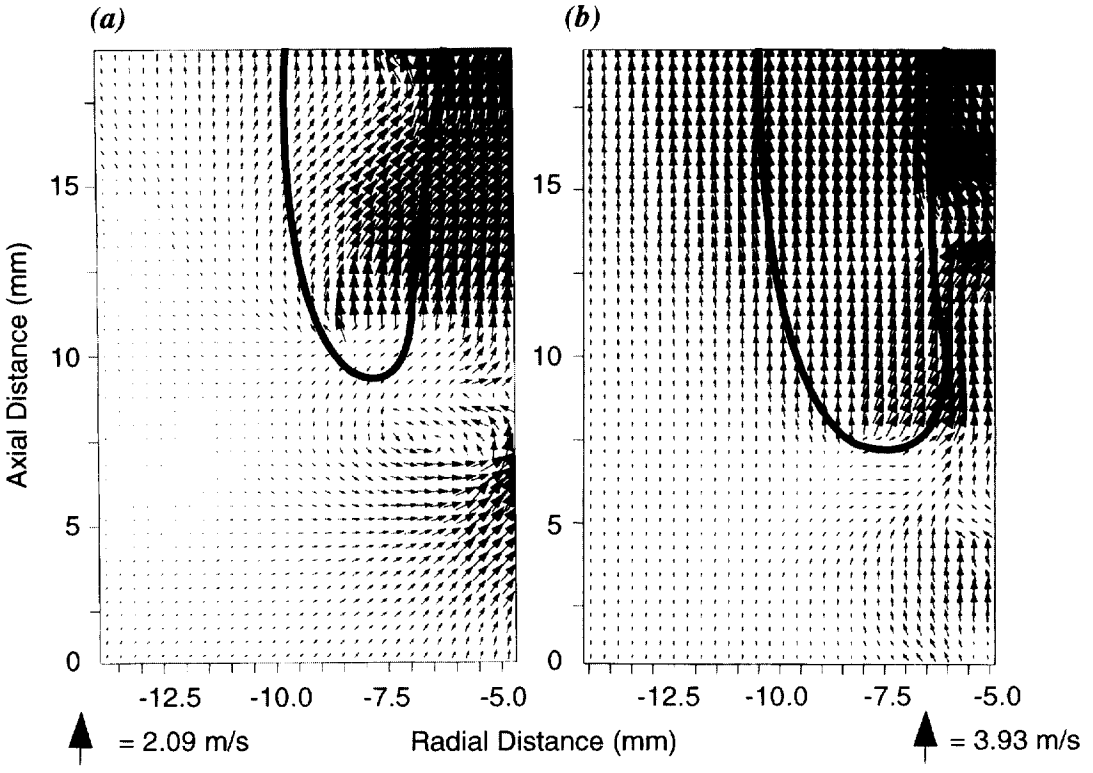

Fig. 5. Instantaneous velocity vector fields in the region of the flame stabilization point. Reynolds number = 7000. The images shown correspond to different laser shots. Region enclosed by heavy solid lines and originating from top of velocity vector field indicates high temperature zone.

shows the low velocities in the stabilization region and divergence of the flow immediately upstream of the flame base. In this case no vortex is present in the stabilization region but entrainment of air into the higher velocity central jet just upstream of the flame is indicated by the inward direction of the velocity vectors.

As described by Muñiz and Mungal [9], conditioning the velocity on the instantaneous flame stabilization point can be used to quantify flow conditions at the flame base. Figure 6 shows profiles of the axial component of velocity, u, along axial lines passing through the flame base. The different symbols correspond to profiles from four different instantaneous velocity fields. Note that each profile has been shifted in the axial direction so that the horizontal axis represents distance from the instantaneous flame base. Figure 6a shows results for the lowest jet Reynolds number of 7000. Similar to the results for a jet with coflowing air, the flow velocity in a free jet decreases to a local minimum at the flame base, and then accelerates across the flame due to volume expansion before asymptoting to a downstream value between 1 and 2 m/s [9]. These observations are consistent with results in a laminar triple flame.

It is important to note that there are several deviations from the laminar case. For example, at the velocity minimum just prior to the flame base, there is a range of velocities and not just a single value equal to S_L, which for CH_4 is 0.43 m/s. It can also be seen that for the profiles shown the minimum value, u_F, is considerably below 0.43 m/s. If an average value for u_F is calculated from the entire data set of 50 images, an average velocity of 0.09 m/s is obtained. The reason for the low value of u_F in the Re = 7000 case will be discussed below.

Finally, it can be seen that the recovery value for the velocity through the flame varies between images, while only a single value is found for the laminar case. The most likely reason for this observation is that velocity fluctuations due

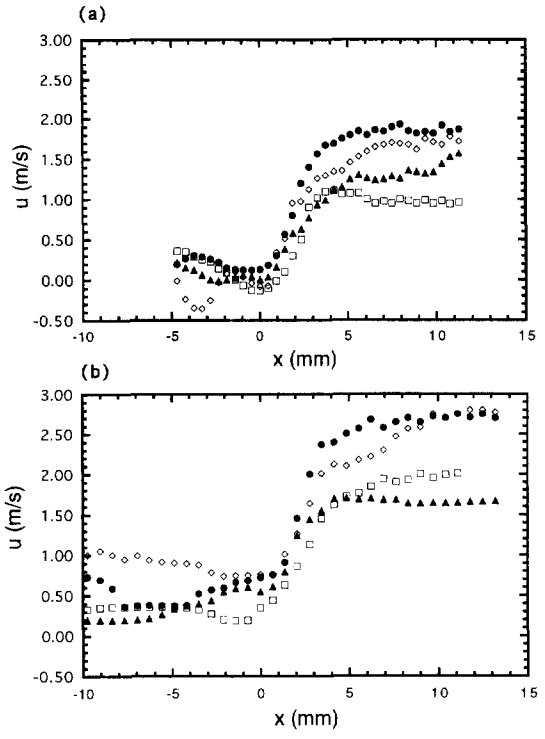

Fig. 6. Instantaneous axial velocity profiles along an axial line through the flame base. (a) Jet Reynolds number = 7000. (b) Jet Reynolds number = 12,000. Different symbols correspond to velocity profiles taken from different images.

to turbulence are superimposed on the downstream recovery velocity, resulting in a range of values. Also, described below, interactions of the flame with turbulence considerably distort the flame structure. This distortion is expected to complicate downstream interactions between the premixed and diffusion flame branches, leading to a temporally varying downstream velocity field.

Conditional axial velocity profiles for the higher Reynolds number of 12,000 are shown in Fig. 6b. As with the Re = 7000 case, the velocity generally decreases to a low value at the flame base before the flow is accelerated across the flame. There is again a range of values for the velocity at the flame base. In this case, however, with the exception of one profile, the velocities at the flame base are higher and near the laminar burning velocity of S_L = 0.43 m/s. Taking an average over 50 profiles gives a value for u_F of 0.5 m/s, which is about 20% higher than S_L. This value is in good agreement with

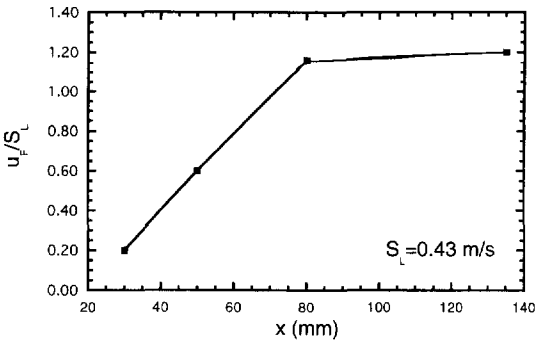

Fig. 7. Variation of normalized average local flow velocity at flame base with axial distance.

the results obtained in lifted flames with coflow at comparable inlet conditions [9]. Conditional velocity profiles for the highest Reynolds-number flame (not shown) are comparable to the results for Re = 12,000 shown in Fig. 6b.

The variation in normalized average velocity, u_F/S_L, with axial distance is shown in Fig. 7. These results were calculated from axial velocity profiles conditional on the flame stabilization point. Results are also included for a Reynolds number of 10,000, which corresponds to a time-averaged lift-off height of 50 mm. The location of the data points along the horizontal axis corresponds to the average visible flame lift-off height. The data show that u_F increases nearly linearly with axial distance to a value about 20% higher than the laminar burning velocity before attaining a nearly constant value for axial distances greater than 80 mm. As described below, the dependence of u_F on flame lift-off height is related to the variation in flame thickness.

Flame Zone Characterization

Typical images of the instantaneous OH distribution are presented in Figs. 8–10 for Re = 7000, 12,000, and 19,500, respectively. The images are false colored to indicate relative levels of the OH concentration, with red indicating the highest levels and deeper blue the lowest level. As seen from previous CH/OH imaging studies in lifted flames, the reaction zone forms in the mixing region adjacent to the central jet [12]. Thus, the region between the two flames zones corresponds to the fuel-rich core of the central fuel jet where, at these upstream locations,

insufficient air has been entrained into the jet to provide a combustible mixture. In each image, the upstream location where the OH first appears defines the flame stabilization point, or flame base. Note that the location of the instantaneous stabilization point varies between images and, in a given image, is generally different on the two sides of the jet.

At the lowest Reynolds number, Fig. 8, the flame zone is relatively thin with an average thickness of about 2 mm. Note from the images that there is considerable variation about this mean value. The images also show evidence of breaks in the flame, for example along the right side of the flame between 35 and 45 mm downstream in Fig. 9c. Radial variations in the flame location are seen from image to image as the flame responds to movement in the central jet boundaries. Similar breaks in the flame, and fluctuations in the radial location, were seen in CH images [6]. The CH/OH imaging further showed that the high CH and OH regions generally coincide in these flames, with the maximum CH being shifted slightly to the fuel-rich side of the OH and the OH distribution being slightly wider than the CH distribution at a given location [12]. Due to the relatively low Reynolds number in Fig. 8, the turbulence levels are low and the flame is not highly convoluted.

It should be noted that the OH concentration decreases to near zero near the top of the images. Previous images have shown that such a decrease is not expected and that the flame, with the exception of localized breaks due to extinction, continues many jet diameters downstream. The apparent disappearance of OH in the present images is due to the combined effects of the decrease in laser sheet intensity near the top of the images (the images were not normalized by the laser sheet intensity distribution) and the use of an image diode in front of the camera which provides little gain (approximately five photoelectrons per incident photon) compared to the micro-channel plate intensifier used in previous work (2000 photoelectrons per incident photon). Thus, the resulting signal falls below the detectability limit of the camera system used in these measurements. In all images presented, however, the OH signal strength and laser sheet uniformity are sufficient in the region of the flame base to provide an accurate representation of the flame structure.

Figure 9 shows typical instantaneous OH distributions for Re = 12,000. In this case the flame is considerably broader and is generally characterized by a more complex structure in the region of the flame base. An average over about 20 images shows the average flame width in this case to have doubled to about 5 mm. It is also quite common to see multiple flame branches, the best examples being in Fig. 9a on the left side of the jet and in Figs. 9b and 9c on the right side of the jet. The images also indicate the highest OH concentrations generally occur nearest the flame base and decrease by almost a factor of 2 downstream. This decrease cannot be accounted for by variations in laser sheet intensity, which varies by less than 20% over the central region of the images where the flame base is generally located. Because of the higher turbulence levels in this higher Reynolds number flow, the flame is considerably more convoluted than at Re = 7000.

Results at Re = 19,500 are shown in Fig. 10. Again, the images show the existence of broad reaction zones near the flame base and multiple reaction zone branches. The average width of the instantaneous reaction zone has increased to nearly 9 mm. Highest relative OH concentration levels again occur nearest the flame base.

DISCUSSION

One objective of the present study is to evaluate the applicability of triple-flame concepts to lifted flame stabilization. Previous CH_4/CH imaging measurements show that the fuel and air are premixed and near stoichiometric conditions immediately upstream of the flame base, with the mixture exceeding the fuel-rich flammability limit toward the central jet and the fuel-lean limit toward the ambient air [5]. These conditions are a necessary requirement for the existence of a triple flame. The conditional velocity profiles obtained here and in Ref. [9] show that the incoming reactants decelerate to a velocity near the premixed laminar flame speed before accelerating across the flame due to volume expansion. These observations are consistent with numerical simulations of laminar

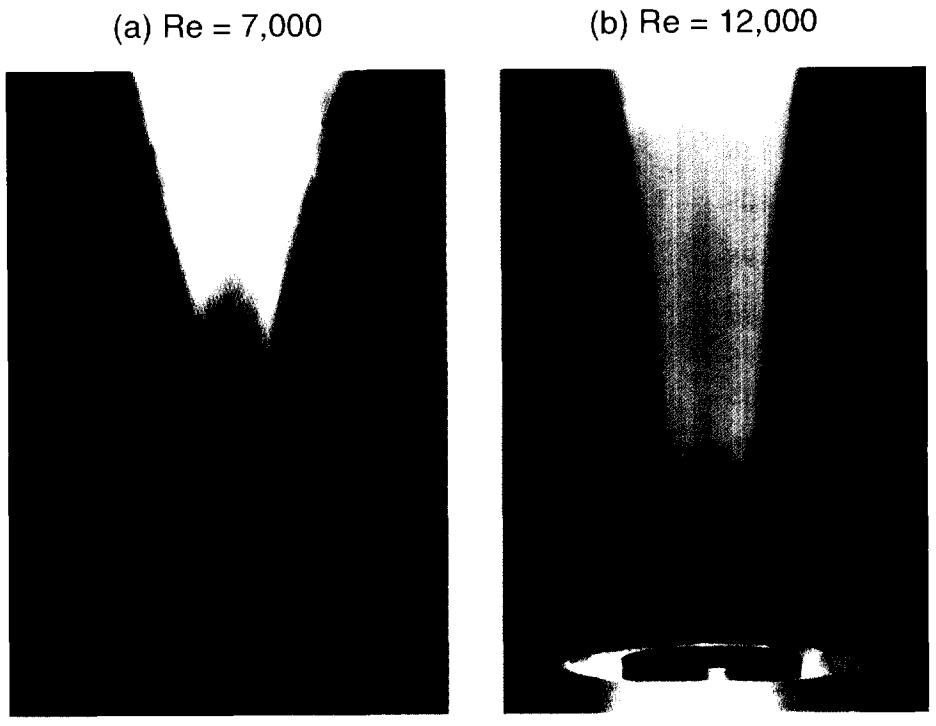

Fig. 2. Photographs of turbulent, lifted CH_4-jet flames. (a) Jet Reynolds number = 7000. (b) Jet Reynolds number = 12,000. (c) Jet Reynolds number = 19,500.

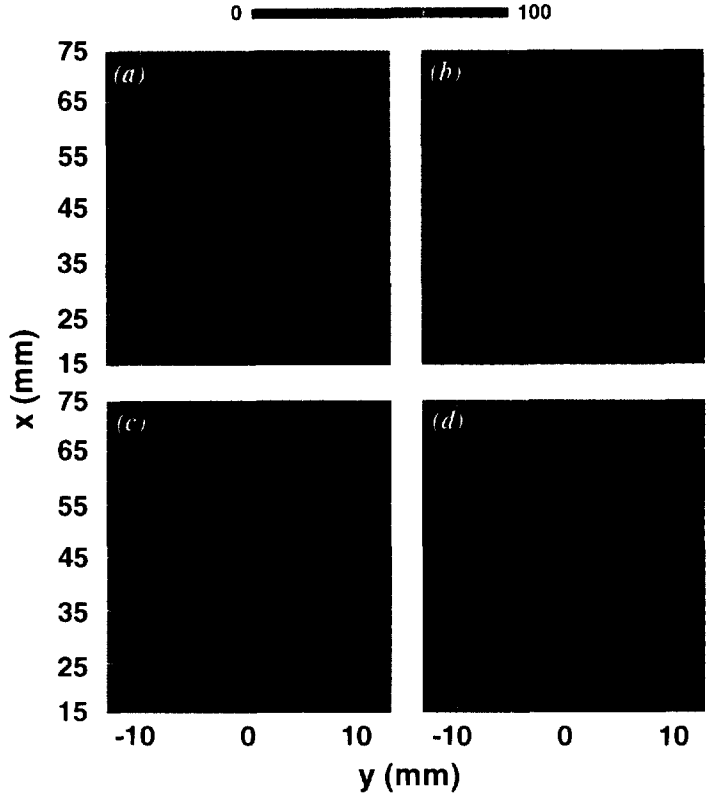

Fig. 8. PLIF images of OH distribution in turbulent, lifted CH_4-jet flame. Reynolds number = 7000.

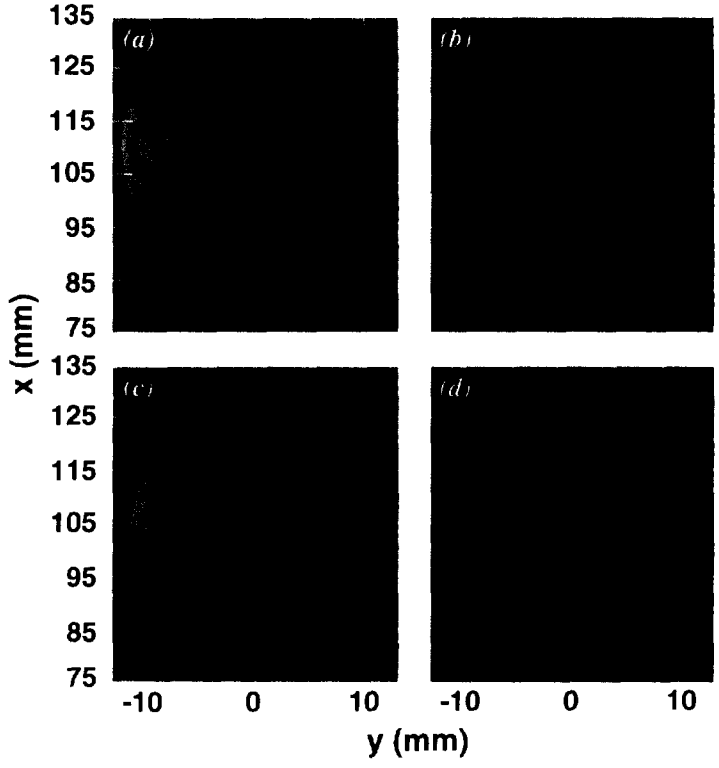

Fig. 9. PLIF images of OH distribution in turbulent, lifted CH_4-jet flame. Reynolds number = 12,000.

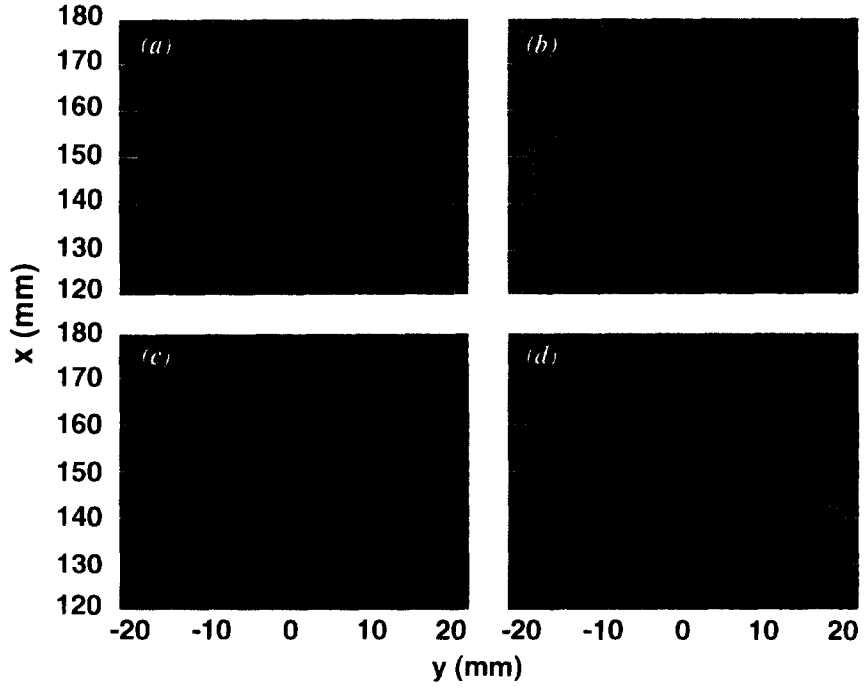

Fig. 10. PLIF images of OH distribution in turbulent, lifted CH_4-jet flame. Reynolds number = 19,500.

triple flames and, in the context of other observations, were taken by Muñiz and Mungal [9] to suggest a downstream diffusion flame that is anchored by a leading-edge flame, which is similar to a triple flame. It is also clear, however, that turbulence causes considerable distortion of the local velocity field and significant differences from the laminar case, which are seen as variations in the velocity minimum at the flame base and in the recovery value of the velocity downsteam of the flame. Such differences suggest that simple extension of laminar triple-flame concepts to turbulent flows may not be straightforward. It is also important to note that the observed velocity profiles are not unique to triple flames. The deceleration of the flow at the flame base is, in fact, due to the expansion of stream tubes upstream of the flame and would be expected where any sudden acceleration of the flow occurs due to volume expansion. Thus, the velocity data do not unambiguously validate the presence of a triple-flame structure.

The OH images also do not corroborate the existence of a triple flame, although it is clear that the reaction zone structure near the flame base is complex and not typical of a classic diffusion flame. This is not entirely unexpected, since the calculations of Veynante et al. [13] show that interactions between triple flames and even a single vortex can cause considerable distortion of the flame structure. Additional measurements will be required, combining the OH images with simultaneous CH imaging, to better establish the presence of fuel-rich and fuel-lean premixed flame branches, and the central diffusion flame structure characteristic of triple flames. In such measurements, the CH, which peaks on the fuel-rich side of the flame, could be used to identify the fuel-rich flame branch while the OH, which peaks slightly on the lean side, would identify the fuel-lean branch. Based on the available experimental data, we have tentatively concluded that flame stabilization at the base of the lifted flames most likely results from the upstream propagation of an ignition front or, given the multiple branches seen in the OH images, multiple fronts propagating against a low velocity flow of partially premixed reactants.

This picture is consistent with recent numerical simulations of the autoignition process in nonuniform reactant mixtures under laminar and turbulent flow conditions [8]. The simulations show that ignition initially occurs along the stoichiometric line where the mixture fraction gradient is below a critical value for quenching. Subsequent propagation of ignition through the reactants then occurs through the propagation of partially premixed ignition fronts. The study further concluded that under some circumstances triple flames may play an important role in the propagation of these fronts. In particular, depending on whether the mixture fraction gradient along the stoichiometric line is uniform or nonuniform, two different types of ignition are observed in the laminar case. With a uniform-mixture fraction gradient, ignition occurs in an initially premixed system and evolves into reaction zones forming a triple-deck structure, with partially premixed flames developing in a direction parallel to the stoichiometric line and a diffusion flame located between them. With a nonuniform-mixture fraction gradient, triple flamelets propagating along the stoichiometric line, from regions of low- to high-mixture fraction gradient, are observed. Simulations for the turbulent case indicate that both of these partially premixed fronts are likely to occur in a turbulent environment due to the inevitable nonuniformities created in the mixture fraction gradient by turbulent mixing.

The measurements presented in Fig. 7 clearly show that the velocity at the flame base increases with the Reynolds number, while the OH images show an increase in reaction zone thickness near the flame base with the Reynolds number. Comparison of these data with CH/CH_4-imaging measurements [5] shows that the increased flame width is consistent with the increased flammable layer width with downstream distance. Shown in Fig. 11 is the variation in the time-averaged width of the flammable region with downstream distance. These widths are determined from about 500 images in both nonreacting flows and reacting flows upstream of the flame stabilization point where the fuel and air have not yet reacted. Here the flammable region is defined as the layer where the CH_4/air is mixed to within the flammability limits for CH_4, which are between CH_4 mole fractions of 0.05 (lean limit) and 0.15 (rich limit) [14]. In the present flows, the flammable layer

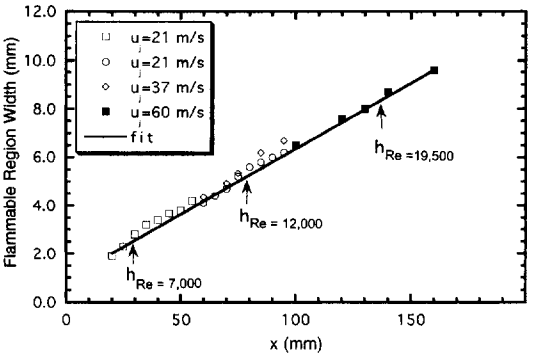

Fig. 11. Variation of time-averaged flammable region width with axial distance in turbulent, lifted CH_4-jet flames. Arrows indicate time-averaged lift-off heights for flames with Reynolds numbers of 7000, 12,000, and 19,500.

occurs in the mixing region adjacent to the central fuel jet. Figure 11 shows that the flammable layer width increases linearly with axial distance. Also indicated by the arrows on the figure are the time-averaged lift-off heights for the three flames studied.

It is important to note that the width of the flammable layer is not constant, but varies significantly from image to image due to variations in the structure of the central fuel jet and the interaction of vortical structures with the jet. Figure 12 shows probability distributions of the instantaneous flammable layer width at the average lift-off heights for the Re = 7000 and 12,000 flames. The distribution for the Re = 19,500 flame (not shown) is similar in shape, with the peak in the distribution shifted to a higher value. In all cases, the widths vary over a considerable range, with larger maximum values at the higher Reynolds number.

The observed fluctuations in the flammable region width are largely related to interactions between vortical structures generated in the jet shear layer and the central jet. Shown in Fig. 13 are three instantaneous radial profiles taken just upstream of the instantaneous flame stabilization point. The top profile corresponds to the leading edge of a vortex that is about to intersect the flame. Highlighted in gray is the region that is within the CH_4 flammability limits. In this case, the width of the flammable layer is relatively thin due to the steep fuel concentration gradient at the outer edge of the vortex. Typically, concentration gradients are highest along the leading edge of the vortex. The second profile corresponds to the trailing edge of a vortex. Here the flammable layer is wider due to the nearly constant concentration plateau region associated with the vortex trailing edge. The third profile corresponds to an instant when no vortex is present in the mixing layer. In this case, the flammable layer width has an intermediate value. It is these interactions with vortical structures that result in the variations in flammable layer width seen in Fig. 12.

The statistics of the flammable region width

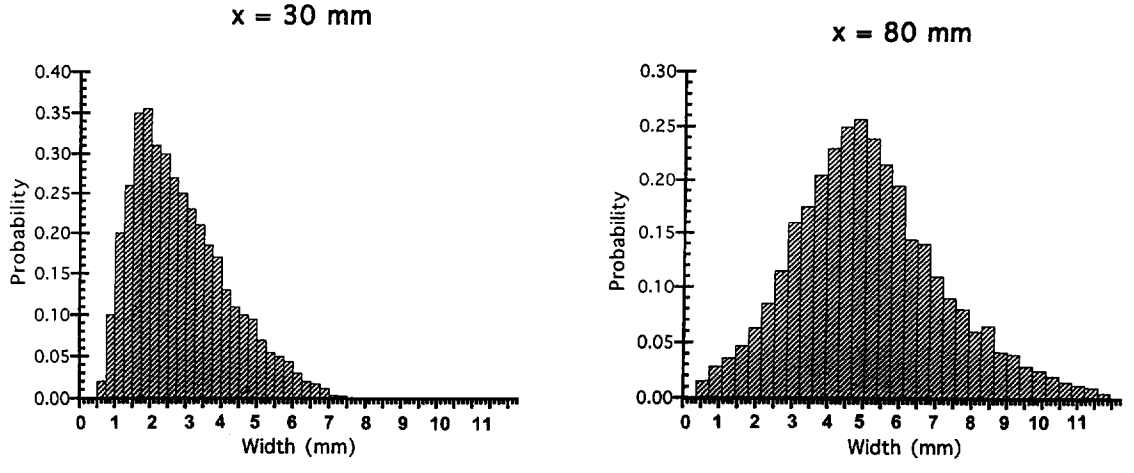

Fig. 12. Probability distributions of the instantaneous flammable layer width. The distribution on the left was taken at the average lift-off height of x = 30 mm for the Reynolds number 7000 flame and the distribution on the right at x = 80 mm for the Reynolds number 12,000 flame.

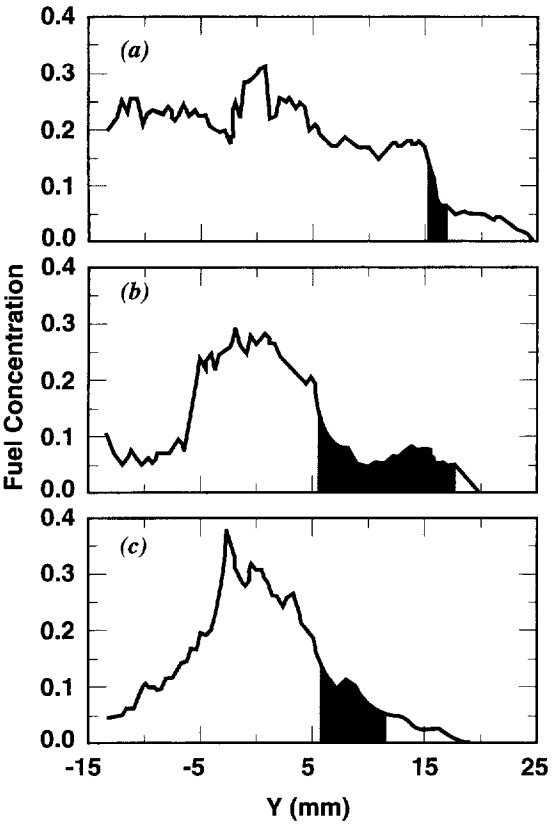

Fig. 13. Instantaneous radial profiles of CH_4 mole fraction in a turbulent, lifted CH_4-jet flame. Reynolds number = 7000. Shaded area indicates region where CH_4 mole fraction is within flammability limits.

can be determined from the probability distributions in Fig. 12. Shown in Table 1 are the mean width, W, the rms fluctuations, W'_{rms}, and the maximum value, W_{max}. A comparison of the mean and maximum values in Table 1 with flame zone widths determined from the instantaneous OH images presented in Figs. 8–10 shows good correspondence. From these results a tentative conclusion can be drawn that the flame fills the flammable layer and that the flame width in the region near the stabilization point is controlled by the width of the flammable layer. Note that this conclusion does not necessarily apply farther downstream where the flame zone exhibits a diffusion flame structure and is considerably thinner than the flame near the stabilization point [8].

TABLE 1

Effect of Reynold's Number on Flammable Region Width

Re	W (mm)	W'_{rms} (mm)	W_{max} (mm)
7,000	2.5	1.4	7.5
12,000	5.3	2.4	11.8
19,500	8.5	4.5	20.0

It is of interest to relate the observed variation in flame thickness to the conditional velocity data presented earlier. It is well known that flame curvature affects upstream transport of both heat and flame radicals [15]. Depending on the sign of the curvature, the burning velocity can be either increased or decreased. If the flame surface is concave toward the reactant mixture, both heat and radicals are focused inward toward the center of curvature, thus increasing upstream transport of heat and radicals to the reactant mixture and effectively increasing the flame propagation speed. This effect is observed at the tip of a bunsen flame where measured flame speeds are up to six times the laminar flame speed [16]. Conversely, if the flame surface is convex toward the reactant mixture, both heat and flame radicals are defocused outward away from the center of curvature, effectively reducing upstream transport of heat and flame radicals, and the flame propagation speed is reduced. Based upon these considerations, it can be speculated that as the flame thickness is reduced due to a reduction in flammable layer thickness, the flame curvature increases and the flame burning velocity decreases. The lower flame velocities measured in the lower Reynolds number flame are thus believed to be due to the reduced flame thickness and increased flame curvature.

This can perhaps be more clearly seen if the results in Fig. 7 are replotted in the form shown in Fig. 14. Here the average local velocity at the flame stabilization point, u_F, normalized by the laminar burning velocity, S_L, is plotted as a function of the mixing layer thickness, L_M, normalized by the premixed flame thickness, L_F. The mixing layer thickness, as defined by Ruetsch et al. [7] for a laminar triple flame in a fuel concentration gradient, is based on the slope of the mixture fraction profile at the stoichiometric point and is given by $L_M = \Delta\xi(\partial\xi/\partial y)_{st}^{-1}$ where ξ is the mixture fraction, $(\partial\xi/\partial y)_{st}$ is the slope of the mixture fraction profile at stoichiometric conditions, $\Delta\xi$ is the

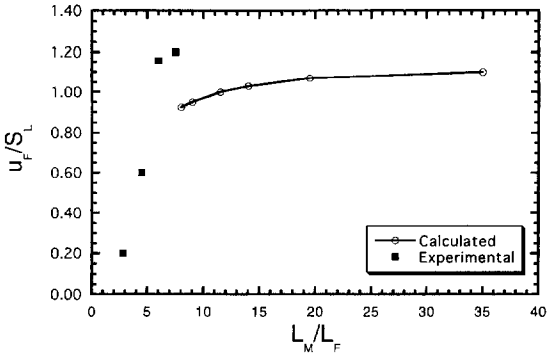

Fig. 14. Average normalized local flow velocity at flame base as a function of normalized mixing layer thickness. Experimental values are indicated by solid symbols. Numerical results (line and open symbols) are from DNS calculations by Ruestch et al. [7].

overall change in mixture fraction across the flame, and y is the distance normal to the stoichiometric surface. The mixing layer thickness is analogous to the flammable layer thickness obtained for the present flames from Fig. 11. The solid line shows the DNS calculations of Ruetsch for a triple flame in laminar flow. Over the range of mixing layer thickness considered in the calculations, u_F/S_L shows only a slight decrease with reduced L_M. This rate of decrease becomes noticeably more rapid at lower L_M. The present data show a maximum velocity approximately 20% higher than S_L and a relatively small dependence on L_M/L_F for $L_M/L_F >$ 5, which is consistent with the calculations. However, the flame speed rapidly decreases as the mixing thickness becomes comparable to the flame thickness. Based on the above discussion, it is speculated that the decrease in u_F as the mixing thickness is reduced is due to curvature effects at the flame base. A more quantitative framework for the effect of flame curvature on flame speed is presented below.

Curvature and Surface Density Effects on Lifted-Flame Stabilization

In this analysis, we assume that lifted flame stabilization is governed by a stoichiometric premixed flame. Among the various processes influencing the propagation of such a flame, we believe that the effects of curvature and related modifications of the flame surface density are dominant.

Flame Curvature Effect

Figures 7 and 14 show that at low Reynolds numbers the fluid velocity ahead of and normal to the flame, S_N, is up to five times smaller than the laminar burning velocity, S_L. As the Reynolds number increases, the fluid velocity S_N increases and asymptotes to a value approximately 20% greater than S_L. We attribute these effects to flame curvature and an increase in flame surface area. Markstein [15] proposed a relationship between the normal burning velocity and the unstrained laminar speed relative to the fresh mixture, including curvature and strain rate effects:

$$\left(\frac{S_N}{S_L} - 1\right) = \frac{L}{S_L}(S_L h + \vec{n}.\nabla u.\vec{n} \tag{1}$$

where L is defined as the Markstein length. The local flame curvature, h, is positive when the flame is concave with respect to the incoming reactant flow, as at the tip of the premixed Bunsen burner flame, and negative when convex with respect to the incoming flow. ∇u is the strain rate tensor of the flow field upstream of the flame front and n is the normal vector to the flame front.

If we assume that the strain rate contribution to the change in burning velocity is negligible, Eq. 1 becomes:

$$S_n = S_L(1 + Lh) \tag{2}$$

The Markstein number, Ma, is defined as $Ma = L/\delta_F$ where δ_F is the laminar flame thickness.

Tseng et al. [17] have estimated Ma as a function of equivalence ratio for various laminar hydrocarbon flames. In the case of a methane flame at stoichiometric conditions, they found Ma to be around 2. Using Eq. 2 the radius of curvature, R = $1/h$, can be expressed as:

$$R = \frac{L}{\frac{S_N}{S_L} - 1} \tag{3}$$

Equation 3 was used to estimate the required radius of curvature needed to account for the observed decrease in fluid velocity at the flame base. From Fig. 7, the measured value of $S_N/S_L.(=U_F/S_N)$ is about 0.2 for the Re = 7000 case. An estimate for the flame thickness was

obtained from the results of Jarosinski [18]. For a stoichiometric, laminar CH_4/air flame, δ_F is estimated to be 0.62 mm based on the mean temperature gradient through the flame, resulting in a Markstein length L = 1.24 mm. Substituting into Eqn. (3) shows that a radius of curvature of 1.6 mm would be required for the laminar burning velocity to decrease from 0.43 m/s to 0.1 m/s. This value is very consistent with the radius of curvature at the flame base for the Re = 7000 case in Fig. 9. (Note that the flame width is about twice the radius of curvature.)

Surface Area Effects

Figure 7 shows that at a high Reynolds number, the average upstream flow of fluid normal to the flame front exceeds the laminar burning speed by about 20%. These results are not surprising for premixed turbulent flames. Shepherd et al. [19] and Goix and Shepherd [20] have found for premixed turbulent flames that the turbulent burning rate increases as the flame surface area increases, as expressed by:

$$S_T = S_L \frac{A_T}{A_L} \tag{4}$$

where A_T/A_L is the increase in flame front surface density. For a flat, turbulent, premixed methane/air flame at stoichiometric conditions they have reported an increase in surface area of nearly 2.19. These measurements were obtained in a uniform, axisymmetric flow at a velocity of 5 m/s with 7% homogenuous turbulence. While a direct comparison between these results and the present measurements is difficult due to the difference in flow conditions, it seems entirely plausible that the relatively small 20% increase observed in S_N can be explained by an increase in the flame surface area due to turbulence.

Relationship to Lifted-Flame Stabilization Theories

As described in the Introduction, previous work by the present authors is most consistent with the premixed flame propagation concepts of Vanquickenborne and van Tiggelen [2]. The theory developed in the previous work is based on the assumption that the local flow velocity is just equal to the turbulent flame propagation speed, S_T, at the flame lift-off position. It is further assumed that the flame stabilizes where the value of S_T is maximum and that this occurs where the fuel/air mixture is stoichiometric. Based on these concepts, Kalghatgi [21] developed an analysis which related the laminar and turbulent flame velocities. Specifically it was shown that the ratio of turbulent to laminar burning velocity varies as the square root of the local turbulence Reynolds number, or

$$S_T^2/S_L^2 = C_1 R_l \tag{5}$$

where C_1 is a constant for a given fuel and R_l is the turbulence Reynolds number based on the integral length scale given by

$$R_1 = u'l/\upsilon_s \tag{6}$$

Here l is the integral length scale and υ_s is the kinematic viscosity at the flame base, which is about 2.3×10^{-5} m^2/s. R_l is related to the turbulence Reynolds number based on the Taylor microscale, R_λ, by the expression

$$R_\lambda = 7R_l^{1/2} \tag{7}$$

Previously obtained LDV data in the present flow shows that the axial velocity (rms) fluctuations, u', at the average liftoff location for the three flames studied, are about 2.2 m/s. Following Kalghatgi, the integral length scale is estimated from $l = C_5 \times x$(C_5 is about 0.07) to be 2.1, 5.6, and 9.45 mm for the Re = 7000, 12,000, and 19,500 flames, respectively. From Eq. 7, these estimates yield values for R_λ of 106, 158, and 200. From Fig. 4 of that paper, the corresponding values of S_T/S_L range between 5 and 10. These values differ considerably from the present values summarized in Figs. 8 and 15.

The discrepancy between the present results and those predicted using Eqs. 5–7 can be understood by considering the basis upon which Eq. 5 was derived. Specifically, from empirical relationships for the time-averaged velocity and concentration distributions in turbulent jets, velocity statistics were obtained at the average flame lift-off height along the time-averaged stoichiometric line. Using the assumption that the flame velocity is equal to the average flow velocity at the flame stabilization point, the relationships provided by Eqs. 5–7 are used to

correlate S_T/S_L as a function of R_λ. What is neglected in the analysis is the large-scale motion of the jet and the resulting movement in the instantaneous flammable region, or stoichiometric line along which the flame is stabilized, and the resulting variation in instantaneous flame stabilization location. Probability distributions of the axial velocity at the time-average flame stabilization point show a range of velocities from slightly negative to a maximum of nearly 15 m/s for the Re = 7000 flame [6]. Similar variations have been measured in the higher Reynolds number flames. Based on the present results, and previous imaging studies in which large-scale fluctuations in the flame lift-off position are observed [6, 8, 22], we propose that the instantaneous flame lift-off position coincides with the time-average value only a small percentage of the time during which the local flow velocity is sufficiently low for the flame to maintain itself against incoming reactants. The large number of velocity realizations, during which time high instantaneous velocities exist at the average stabilization location and the flame is stabilized elsewhere in a lower velocity region, heavily weight the time-average velocity statistics toward values considerably higher than the actual flow velocity at the flame base. The recent development of PIV and the ability to condition the velocity statistics on the location of the flame stabilization point provide the experimental means to account for fluctuations in the flame stabilization location that are difficult to identify using point measurement techniques.

As a final note, the measurement of velocities at the instantaneous flame base comparable to the premixed laminar flame speed are consistent with the presence of a triple flame at the flame stabilization point which anchors a diffusion flame farther downstream. These results, taken in conjunction with previous measurements in the region of the flame base, further suggest that the ability of a lifted flame to stabilize at a given location requires two criteria to be met. First, the fuel and air must be premixed and near stoichiometric conditions to allow the flame to propagate against the local flow. This criterion is based on a previous study using simultaneous CH, CH_4, and temperature imaging to study conditions at the flame stabilization point [5]. Second, as shown by the above data, the local flow velocity must be sufficiently low and near the premixed laminar flame speed. Although the OH PLIF images do not corroborate the presence of a triple flame, simultaneous planar imaging of OH and CH is currently being planned to provide a more detailed study of the flame structure at the stabilization point.

SUMMARY AND CONCLUSIONS

Particle image velocimetry was used to study the velocity field in lifted, turbulent CH_4-jet flames over a range of Reynolds numbers from 7000 to 19,500. The results show that flow velocities at the instantaneous stabilization point are considerably below the expected turbulent-flame speed and show a Reynolds number dependence. At the lowest Reynolds number, the average velocity at the stabilization point is nearly a factor of 5 below the premixed laminar flame speed. This average velocity asymptotes to a value about 20% higher than the premixed laminar flame speed at the highest Reynolds number. Planar images of OH show that the flame zone structure near the stabilization point is highly dependent on Reynolds number. Comparison of the OH images with previous measurements shows that the flame thickness is determined by the width of the flammable region. At a low Reynolds number, the flame is stabilized nearest the jet exit where the flammable layer is thin, resulting in a thin flame zone. At an increased Reynolds number, the stabilization point is located farther downstream where the flammable region is wider, resulting in a correspondingly wider flame zone. It is proposed that the lower flame speeds observed at decreasing Reynolds number are related to thinning of the flame zone as Reynolds number is reduced, which results in greater curvature of the flame base. This increased flame curvature effectively defocuses the transport of heat and flame radicals to reactants upstream of the propagating flame front, resulting in reduced local flame speeds at the base.

Measured velocities at the instantaneous flame base are comparable to the premixed laminar burning velocity. These results, taken in

conjunction with previous imaging measurements, suggest that the ability of a lifted flame to stabilize at a given location requires two criteria to be met. First, the fuel and air must be premixed and near stoichiometric conditions to allow the flame to propagate against the local flow. Second, the local flow velocity must be sufficiently low and near the premixed laminar flame speed. The OH PLIF images show considerable distortion of the flame structure due to turbulence, which makes it difficult to identify the flame with the triple-flame structure found in laminar flows. The images do show a complex structure at the flame base with multiple reaction branches. From the available experimental data, flame stabilization at the base of the lifted flames most likely results from the upstream propagation of an ignition front or, given the multiple branches seen in the OH images, multiple fronts propagating against a low velocity flow of partially premixed reactants.

This research was supported by the U.S. Department of Energy, Office of Basic Energy Sciences, Division of Chemical Sciences. The authors would like to acknowledge the assistance of Tony Whitworth in the PIV system assembly and data acquisition.

REFERENCES

1. Pitts, W. M. (1988). *Twenty-Second Symposium (International) on Combustion*, The Combustion Institute, Pittsburgh, pp. 809–816.
2. Vanquickenborne, L., and van Tigglen, A., *Comb. Flame* 10:59–69 (1966).
3. Peters, N., and Williams, F. A., *AIAA J.*, 21:423–429 (1983).
4. Byggstoyl, S., and Magnussen, B. F., *Fourth Symposium on Turbulent Shear Flow* (L. J. S. Bradbury, F. Durst, F. W. Schmidt, and J. H. Whitelaw, Eds.), Karlsrühe, Germany 1983, pp. 10.32–10.38.
5. Schefer, R. W., Namazian, M., and Kelly, J., *Combust. Flame* 99:75–86 (1994).
6. Schefer, R. W., Namazian M., and Kelly, J. (1994). *Twenty-Fifth Symposium (International) on Combustion* The Combustion Institute, Pittsburgh, p. 1223–1231.
7. Ruetsch, G. R., Vervisch, L., and Linan, A. *Phys Fluids* 7:1447–1454 (1995).
8. Domingo, P., and Vervisch, L. (1996). *Twenty-Sixth Symposium (International) on Combustion*, The Combustion Institute, Pittsburgh, p. 233–240.
9. Muniz, L., and Mungal, M. G. *Combust. Flame* 111: 16–31 (1997).
10. Barlow, R. S., and Collignon, A. (1991). AIAA Twenty-Ninth Aerospace Sciences Meeting, Reno, NV, January 7–10, Paper No. AIAA 91-0179.
11. Mungal, M. G., Lourenco, L. M., and Krothapalli, A., *Combust. Sci. Technol.* 106:239–265 (1995).
12. Schefer, R. W., Namazian, M., and Kelly, J. (1990). *Twenty-Third Symposium (International) on Combustion*, The Combustion Institute, Pittsburgh, p. 669–676.
13. Veynante, D., Verisch, L., Poinsot, T., Liñán, A., and Ruetsch, G., *Studying Turbulence Using Numerical Databases* (V. P. Moin and W. C. Reynolds, Eds.), Center for Turbulence Research, Stanford University, 1994, pp. 55–73. 1994.
14. Lewis, B., and Von Elbe, G., *Combustion, Flames and Explosions of Gases*, 3rd ed., Academic Press Inc., Orlando, FL, 1987.
15. Markstein, G. H., *Nonsteady Flame Propagation*, Macmillan, New York, 1964.
16. Echekki, T., and Mungal, M. G. (1990). *Twenty-Third Symposium (International) on Combustion*, The Combustion Institute, Pittsburgh, p. 455–787.
17. Tseng, L. K., Ismail, M. A., and Faeth, G. M., *Combust. Flame* 95:410–426 (1993).
18. Jarosinski, J., *Combust. Flame* 56:337–342 (1984).
19. Shepherd, I. G., Cheng, R. K., and Goix, P. J. (1990). *Twenty-Third Symposium (International) on Combustion* The Combustion Institute, Pittsburgh, p. 781–787.
20. Goix, P. J., and Shepherd, I. G., *Combust. Sci. Technol.* 91:191–206 (1993).
21. Kalghatgi, G. T., *Combust. Sci. Technol.* 41:17–29 (1984).
22. Pitts, W. M. (1990). *Twenty-Fourth Symposium (International) on Combustion*, The Combustion Institute, Pittsburgh, p. 661.

Received 29 July 1996; accepted 12 March 1997.